IEEE Access
Multidisciplinary ⋮ Rapid Review ⋮ Open Access Journal

Received 6 February 2023, accepted 28 February 2023, date of publication 3 March 2023, date of current version 8 March 2023.

Digital Object Identifier 10.1109/ACCESS.2023.3252003

RESEARCH ARTICLE

A Closed-Loop Micro-Ultrasonic Motor Control System With Extremum Seeking

MOHAMED M. KHALIL[1,2], (Graduate Student Member, IEEE), NAOYA MASUDA[1], KOTARO TAKAYAMA[1], AND TOMOAKI MASHIMO[3], (Member, IEEE)

[1]Department of Mechanical Engineering, Toyohashi University of Technology, Toyohashi 441-8580, Japan
[2]Department of Mechanical Engineering, College of Engineering and Technology-Cairo Campus, Arab Academy for Science, Technology and Maritime Transport, Cairo 4471344, Egypt
[3]Graduate School of Natural Science and Technology, Okayama University, Okayama 700-8530, Japan

Corresponding author: Mohamed M. Khalil (mohamed.mostafa.abdelaziem.khalil.km@tut.jp)

This work was supported in part by the Japan Society for the Promotion of Science (JSPS) KAKENHI under Grant 22H01446.

ABSTRACT Microactuators are an essential technology to revolutionize existing micromachines, but making them closed-loop controlled with an internal sensor is a great challenge due to the limited size of the components. In this paper, we build a micro-ultrasonic motor in the 2-3 mm scale, combine it with a tunneling magneto resistance (TMR) sensor with dimensions of 1.4 mm × 1 mm, and construct a closed-loop system with a control algorithm. It is currently the smallest rotary actuator-sensor system assembled into a size with a height of 3.2 mm, a width of 3.2 mm, and a length of 5 mm. In the system, we attempt to solve a steady-state error problem for the micro-ultrasonic motor's internal parameter changes, such as a temperature rise and the resonant frequency variation. A model-free, real-time-adaptive extremum seeking controller (ESC) that continuously tracks and localizes the optimum driving frequency is implemented into the system for the desired rotation with minimum steady-state error. Although the controller is simply designed, experiments show a good accordance between the resulting angular velocity and the reference.

INDEX TERMS Piezoelectric actuators, ultrasonic motors, micromotors, closed-loop control, extremum seeking controller, temperature disturbance.

I. INTRODUCTION

Micro actuators are needed for a variety of purposes, ranging from practical applications such as medical and industrial endoscopes to scientific investigations such as controlling biomimetic microrobots. Downsized to 2-3 millimeter scale, electromagnetic actuators that dominate at macro-scale diminish their power due to their scaling law [1], [2]. Furthermore, they involve several technical problems to miniaturize the components, such as coils, permanent magnets, and bearings. Instead, piezoelectric ultrasonic motors perform at such a scale as the most prominent microactuators because of their high power density and good machinability [3], [4]. Despite the great scalability, they have obvious nonlinear and time-varying characteristics that complicate their models for control.

The associate editor coordinating the review of this manuscript and approving it for publication was Michail Kiziroglou.

Controlling regular-sized traveling-wave ultrasonic motors (TWUSMs) are classified into two states: transient and steady states. The transient response of ultrasonic motors is in good agreement with the model based on the first-order system [5], [6]. Although the response speed depends on the moment of inertia, ultrasonic motors can reach the desired velocity within milliseconds as estimated in the model [7], [8]. A typical application of controlling the transient state is the autofocusing feature in camera lenses, and the implemented motor provides good controllability with a quick response and high accuracy.

In the steady states, the models of ultrasonic motors are much more complicated than those of the transient state [7], [9], [10], [11], [12]. For example, after starting to spin with a constant voltage, open-loop ultrasonic motors enlarge the steady-state error of the angular velocity nonlinearly with time [13]. The physical phenomena that occur in ultrasonic motors are mainly due to the mechanical damping of the

stator, the dielectric loss of the piezoelectric elements, and the friction at the stator-rotor interface. These dissipations result in a temperature rise that affects the stiffness of the piezoelectric material and the natural frequency of the stator. None of the ultrasonic motors, therefore, can retain a desired steady state without control.

There were many attempts to develop control strategies for manipulating the angular velocity of ultrasonic motors. Classical PI and PID controllers [14], [15], fuzzy logic controllers [16], [17], neural network controllers [18], and adaptive controllers [19], [20], have been proposed as control algorithms for ultrasonic motors. For instance, classical controllers are simple and offer a wide stability margin but fail to cope with time-varying systems if not equipped with self-learning capabilities or an auto-tuning algorithm. On the contrary, a fuzzy logic controller can deal with nonlinear systems, but it relies too much on the designer's knowledge to define fuzzy rules. Both neural networks and adaptive controllers can adapt to the time-varying parameters of systems, thus suppressing the disadvantages of the classical and fuzzy controllers. However, the use of the neural network requires intricate online training iterations for output optimization. Although adaptive controllers seem promising, most of the existing methodologies are based on the model reference adaptive control (MRAC) approach. As most identified models of ultrasonic motors are based on classical linear system identification, estimating an accurate model for the MRAC approach is very complex. Therefore, designing a model-free adaptive controller that can handle the nonlinearity of ultrasonic motors and converge quickly to the optimum state is desirable.

We have studied micro-ultrasonic motors, which is one of the most powerful actuators in a 2-3 mm scale [4]. Although it is still open-loop, these micromotors have represented a possibility toward microrobot applications, such as insect-scale robots [21], [22] and micro aerial vehicles [23]. For further development of microrobots, constructing a closed-loop was absolutely necessary, but there was no tiny sensor that can be attached to the micro-ultrasonic motor. In other words, existing commercially-available rotary sensors, e.g., optical and hall sensors, were much larger than the micromotors and spoiled the advantage of the micromotors. Recently, a sensor company has provided us with the smallest tunneling magneto resistance (TMR) sensor that can be used as a rotary sensor. The size of this TMR sensor, measuring 1.4 mm $\times$ 1 mm $\times$ 0.6 mm, is very suited for the size of micro-ultrasonic motors. In this paper, we propose the smallest closed-loop system using a micro-ultrasonic motor and the TMR sensor. Because the temperature dependency of the micro-ultrasonic motor is unpredictable, we employ an adaptive model-free controller that can handle the nonlinear characteristics by controlling the applied voltages.

The main contributions of this paper are summarized as follows.

- The smallest closed-loop system of the rotary actuator and sensor is presented and demonstrated.
- An extremum seeking controller (ESC) that stabilizes the steady-state angular velocity by seeking an optimum value is implemented in the smallest system.

In the rest of this paper, Section II describes the model of the ultrasonic motors and formulates the relationship between the temperature and the motor's parameters. Section III shows the fundamental characteristics needed for control and presents the working principle of the ESC. Section IV demonstrates the closed-loop feedback system and confirms the performance of ESC through experiments. Section V concludes the paper and points out possible future work for the proposed approach.

II. MODELING AND FORMULATION OF PHENOMENA

A. MODELING OF THE MOTION

Fig. 1(a) shows the stator model of the micro-ultrasonic motor. The stator is composed of a phosphor bronze cube with a hole and four piezoelectric plates bonded to the sides of the cube. It is considered an electromechanical energy converter, in which the input voltages are converted into mechanical motion. When two sinusoidal voltages with amplitude E, frequency f, and a 90° phase shift are applied to the piezoelectric elements, a traveling wave is produced on the inner surface of the stator circumferentially. The mass particles on the surface where the traveling wave moves generate an elliptical motion in the stator-rotor interface, spinning the rotor by frictional contact force as illustrated in Fig. 1(b). For a given voltage $V = E\sin(2\pi ft)$, the motion of that mass particle can be modeled as a mechanical system consisting of springs and dampers elements in the horizontal and vertical directions. Fig. 1(c) shows the modeled mechanical system. In this system, we define the mass of the particle by m_s, the horizontal and vertical spring coefficients by k_x and k_y, respectively, and the horizontal and vertical damping coefficient by c_x and c_y, respectively.

Besides, Fig. 1(c) shows all the components of the micro-ultrasonic motor, which consists of a stator, a rotor, and a preload mechanism. In these, a microspring presses the rotor against the stator. The rotor absorbs the vibration energy from the stator by friction and converts it into its rotational motion. The energy absorption is determined by the preload force F_N between the stator and rotor as detailed in [24]. By assuming the stator-rotor contact as an energy absorption factor with damping coefficients b_x and b_y in the horizontal and vertical direction, respectively, the equation of motions of the stator's vibration can be expressed as

$$\begin{aligned} m_s\ddot{x} + (c_x + b_x)\dot{x} + k_x x &= F_x \\ m_s\ddot{y} + (c_y + b_y)\dot{y} + k_y y &= F_y \end{aligned} \tag{1}$$

where F_x and F_y are given by

$$\begin{aligned} F_x &= F_0\, cos(\omega t) \\ F_y &= F_0\, sin(\omega t) \end{aligned} \tag{2}$$

where F_o is the net force applied from the stator to the rotor and ω is the vibration frequency. The net force can be

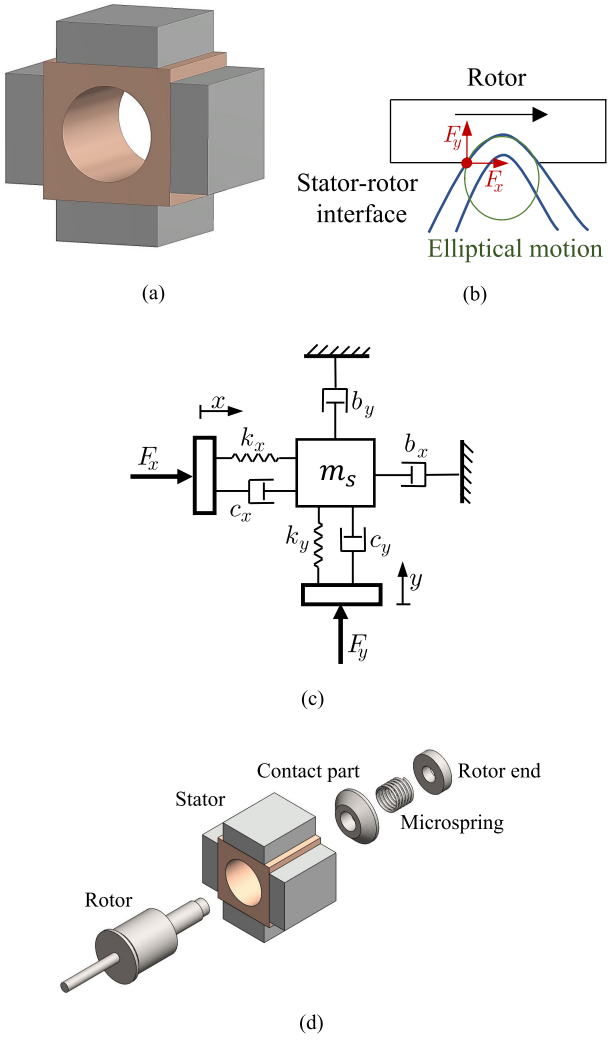

FIGURE 1. (a) The schematic of the stator for the micro-ultrasonic motor, (b) stator generates an elliptical motion on the stator–rotor interface and transfers a driving force to the rotor, (c) the mechanical model of the micro-ultrasonic motor, and (d) components of the micro ultrasonic motor.

derived by

$$F_0 = n_1 V - F_N \tag{3}$$

where n_1 is the coupling factor that represents the electromechanical (voltage-to-force) conversion.

The modeled system is well known as a forced harmonic vibrating system in which driving the system at its resonant state maximizes the vibration amplitudes [25]. The system is at a resonant state if the applied frequency ω equals to its natural frequency ω_n which can be calculated as follows

$$\omega_n = \sqrt{\frac{k_x}{m_s}} = \sqrt{\frac{k_y}{m_s}} \tag{4}$$

The steady-state response of the vibrating system in the horizontal and vertical axis can be derived as

$$\begin{aligned} x(t) &= \frac{F_0}{[(k_x - m_s\,\omega^2)^2 + (c_x + b_x)^2\,\omega^2]^{\frac{1}{2}}}\, cos(\omega t - \phi_1) \\ y(t) &= \frac{F_0}{[(k_y - m_s\,\omega^2)^2 + (c_y + b_y)^2\,\omega^2]^{\frac{1}{2}}}\, sin(\omega t - \phi_2) \end{aligned} \tag{5}$$

where ϕ_1 and ϕ_2 are given by

$$\begin{aligned} \phi_1 &= tan^{-1}\left[\frac{(c_x + b_x)\,\omega}{k_x - m_s\,\omega^2}\right] \\ \phi_2 &= tan^{-1}\left[\frac{(c_y + b_y)\,\omega}{k_y - m_s\,\omega^2}\right] \end{aligned} \tag{6}$$

As the elliptical motion starts, the mass particle moves with the peak horizontal velocity at the top point. As the rotor is in contact with the top point, it spins at an angular velocity Ω. The peak horizontal velocity $\dot{x}_{max}$ can be derived by differentiation (5) as follows

$$\dot{x}_{max} = \frac{F_0\,\omega}{[(k_x - m_s\,\omega^2)^2 + (c_x + b_x)^2\,\omega^2]^{\frac{1}{2}}} \tag{7}$$

By dividing both the numerator and denominator of (7) by k_x and substituting (4) into it, the peak horizontal velocity can be expressed as

$$\dot{x}_{max} = \frac{F_0\,\omega/k_x}{[[1 - (z)^2]^2 + [\frac{d_x}{m_s\,\omega_n} z]^2]^{\frac{1}{2}}} \tag{8}$$

where d_x is defined as the total damping in the horizontal direction ($d_x = c_x + b_x$), while z is defined as the frequency ratio of the system that can be expressed as

$$z = \frac{\omega}{\omega_n} \tag{9}$$

By transforming this peak horizontal velocity into the rotor's angular velocity, Ω can be computed as

$$\Omega = \frac{\dot{x}_{max}}{r} \tag{10}$$

where r is the effective radius of the micro ultrasonic motor.

Substitute (8) into (10), the rotor's angular velocity can be expressed as

$$\Omega = \frac{F_0\,\omega}{k_x r[[1 - (z)^2]^2 + [\frac{d_x}{m_s\,\omega_n} z]^2]^{\frac{1}{2}}} \tag{11}$$

The above equation is used when the moment of inertia is very small or neglected, i.e., no load is attached to the rotor. In other cases, the angular velocity can be calculated using the equation of motion for rotor dynamics as follows

$$I\,\dot{\Omega} - \nu_m\,\Omega = \tau - \tau_l \tag{12}$$

where τ is the applied torque, I is the moment of inertia, ν_m is the damping coefficient, and τ_l is the load torque that acts against the motor torque.

B. MODELING OF TEMPERATURE VARIATION

The existing mathematical models of ultrasonic motors can estimate the response of the angular velocity under certain input voltages and torques; however, they cannot derive the steady-state error without considering the temperature of the stator. It is essential to model how the temperature rise affects the dynamic and steady-state characteristics of the rotation in the time domain. The heat dissipation generated in the micro-ultrasonic motor is due to the dielectric loss of the piezoelectric materials q_e, the mechanical damping of the stator q_m, and the friction loss between the stator and the rotor q_f. The total power dissipation q in the motor is the sum of these factors:

$$q = q_e + q_m + q_f \tag{13}$$

By subtracting the power q_d that radiates to the ambient air from the total dissipation q, the change in the stator's temperature T is expressed using the conversion of energy:

$$q - q_d = m\, c_p \frac{dT}{dt} \tag{14}$$

where m and c_p are the mass and the specific heat of the stator, respectively. The heat that dissipates to the ambient air with a temperature of T_0 by convection through the surface area A_s can be expressed as

$$q_d = K_T A_s (T - T_0) \tag{15}$$

where K_T is the heat convection coefficient. Eq. (14) shows that the surface temperature of the stator reaches the steady-state when the radiation q_d is equal to the total loss q. By substituting (15) into (14), the stator temperature T is obtained as follows:

$$T = T_0 + \frac{q}{K_T\, A_s}(1 - e^{-\frac{t}{\gamma}}) \tag{16}$$

where $\gamma = mc_p/K_T A_s$ is the heat dissipation constant. When voltages with an amplitude E are applied, the total power loss q can be identified as $q = n_2 E$, and (16) can be rewritten as

$$\Delta T = \frac{n_2 E}{K_T\, A_s}(1 - e^{-\frac{t}{\gamma}}) \tag{17}$$

From (17), we can estimate how the input voltages affect the temperature rise.

C. RELATIONSHIP BETWEEN TEMPERATURE, NATURAL FREQUENCY, AND ANGULAR VELOCITY

It is known that, in existing ultrasonic motors, the temperature rise lowers the stiffness of the piezoelectric materials, resulting in a decrease in the natural frequency. The micro-ultrasonic motor is more sensitive to temperature variation because the volume ratio of the piezoelectric material to the stator is larger than normal ultrasonic motors. Although the relationship between the temperature rise and the natural frequency is nonlinear, it can be approximated as a linear function in the range that the ultrasonic motor operates. Taking k_x previously described in the mechanical model of the motor in (1) as an example, the degradation of the spring constant due to temperature can be expressed as follows

$$k_x = k_{x0} - \alpha_x (T - T_0) \tag{18}$$

where k_{x0} is the original spring constant at $T = T_0$ and α_x is the coefficient of spring degradation.

By substituting (17) into (18), we got

$$k_x = k_{x0} - \alpha_x \frac{n_2 E}{K_T\, A_s}(1 - e^{-\frac{t}{\gamma}}) \tag{19}$$

The change in the spring constant causes a shift in the natural frequency of the mechanical system expressed in (4) as follows

$$\omega_n = \sqrt{\frac{k_x}{m_s}} = \sqrt{\frac{k_{x0} - \alpha_x \frac{n_2 E}{K_T\, A_s}(1 - e^{-\frac{t}{\gamma}})}{m_s}} \tag{20}$$

Eq. (9) shows that a shift downward of the natural frequency enlarges the frequency ratio z of the system. Eq. (11) predicts that enlarging z will diminish the angular velocity of the rotor. To validate this point, we plot Eq. (11) with z as a variable while all other elements are kept constant at a unity value as shown in Fig. 2. The graph is compliant with the analysis of a damped forced harmonic system in [25].

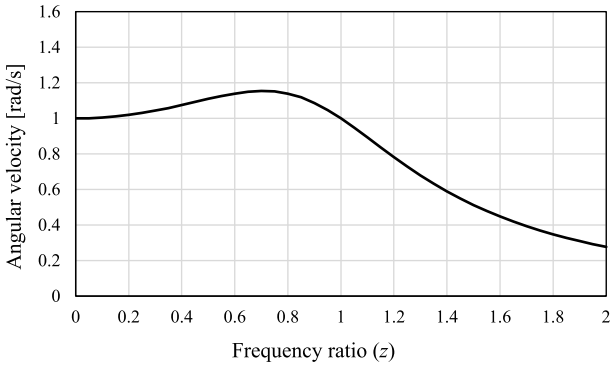

FIGURE 2. Change in the rotor's angular velocity when the frequency ratio varies.

At the initial configuration of the system, we manually adjust the driving frequency to match the natural frequency to operate the motor at the resonant state ($z = 1$). After the temperature rises, the natural frequency drops, and the frequency ratio z becomes larger than 1. As a consequence, the system is no longer operated at the resonant state, and the angular velocity drops.

III. DESIGN OF THE CONTROLLER

A. EXPERIMENTS FOR DESIGNING THE CONTROLLER

Obtaining a good controller for a micro-ultrasonic motor is a key in this study, but it is as hard as accurately modeling the system. In principle, there are three manipulated variables to control the angular velocity: the voltage amplitude, the frequency, and the phase difference of the input signals [26]. In these, changing the driving frequency gives a more flexible

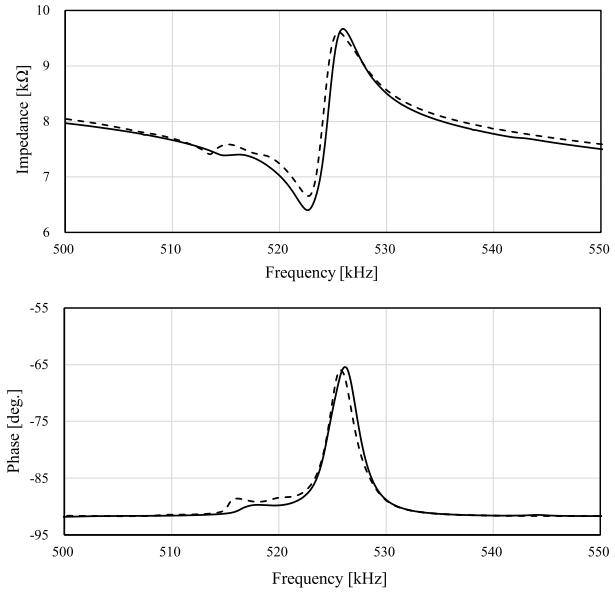

FIGURE 3. Impedance-frequency characteristic of the micro-ultrasonic motor.

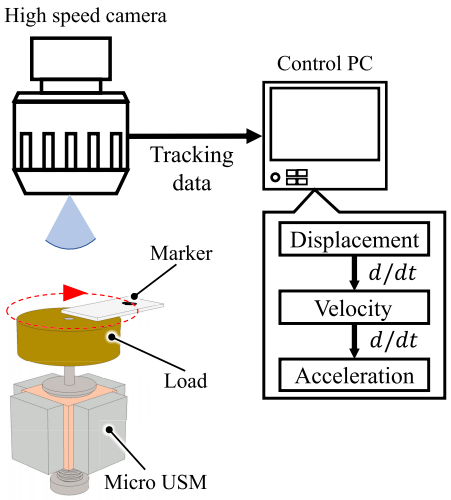

FIGURE 4. Illustration of the speed measurement setup of the micro-ultrasonic motor. A marker is attached to the load to facilitate the tracking motion by the high-speed camera.

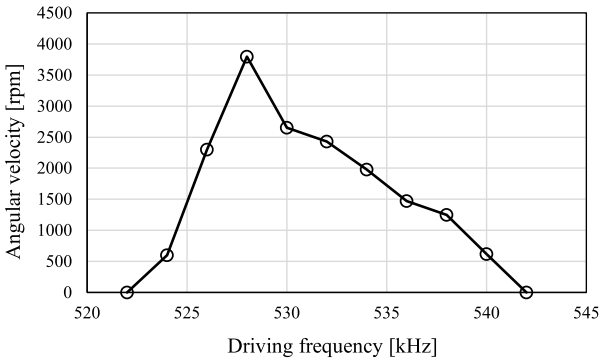

FIGURE 5. The relationship between the angular velocity and the driving frequency.

range from a low-speed domain and is widely applied for the motion control of ultrasonic motors.

The frequency characteristic, i.e., the variation in the angular velocity with the input frequency, is evaluated experimentally. In the measurement of the angular velocity, we manipulate the frequency while the two input sinusoidal voltages keep constant at 100 V_{p-p}. These input voltages are generated using a wave generator with two channels (WF1974, NF Corp., Yokohama, Japan) and amplified by power amplifiers (BA4825, NF Corp., Yokohama, Japan). Prior to this experiment, the resonant frequency of the stator was electrically measured by an impedance analyzer (IM3570, Hioki E. E. Co., Japan) at a controlled room temperature of 25°C. It measured 525 kHz as shown in Fig. 3.

To measure the angular velocity, a small bronze disc with a diameter of 3 mm and a thickness of 1 mm is attached to the end of the rotor as a load, as shown in Fig. 4. A marker is also attached to the disc to facilitate the speed measurement. The motor angular velocity is measured using a high-speed camera with an image resolution of 320 × 240 pixels at 2000 fps (VW-9000, Keyence Co., Tokyo, Japan). The time-history data of the angular displacements are accumulated from the marker's movement in the images, and angular velocity and acceleration can be obtained by performing the time derivation of these data. Fig. 5 shows the frequency characteristic of the steady-state angular velocity when the constant voltages are applied. The angular velocity peaks at 528 kHz, which is slightly higher than that of the resonant frequency of the stator without the rotor. That is because the preload force attached to the rotor enhances the stiffness of the stator, and it shifts the resonant frequency upward [27].

To evaluate the extent of the actual temperature rise, we measure the time-history response of the stator's temperature during the motor operation. The surface temperature of the stator is measured by a spot finder IR camera (Xi 400, Optris Co., Germany) while the room temperature is constant at 25°C. Fig. 6 shows the time-history of the increment in the temperature ΔT when the amplitudes of 80, 100, and 120 V_{p-p} are applied. The experimental results are in good agreement with the simulation results of the temperature variation model shown in (17). Table 1 summarizes the parameters necessary for the simulation.

We also examine how the temperature rise of the stator relates to the natural frequency as previously explained in section II-C experimentally. In this experiment, the stator is heated by flowing warmed air until $\Delta T = 10$°C, while the resonant frequency is continuously recorded by the impedance analyzer. Fig. 7 shows the variation in the natural frequency of the stator when the temperature increases. The result shows that the resonant frequency is roughly linear to the temperature. From Fig. 6 and Fig. 7, we can predict that the temperature rise enlarges the steady-state error as it alters the natural frequency of the stator. Because

TABLE 1. Simulation parameters for the temperature variation in the micro-ultrasonic motor.

Quantity	Symbol	Value
Volt/temp. constant	n_2	1.28×10^{-6}
Stator mass	m	0.0001 kg
Specific heat	c_p	0.435 kJ/kg °K
Surface area	A_s	3.7×10^{-6} m^2
Heat conv. coeff.	K_T	3.3

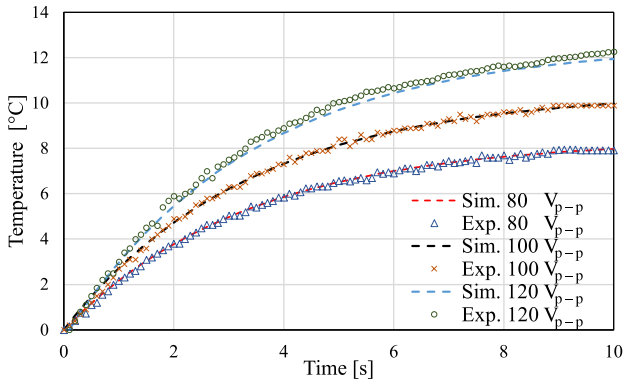

FIGURE 6. Temperature variation in the stator while three different values of input voltages are applied.

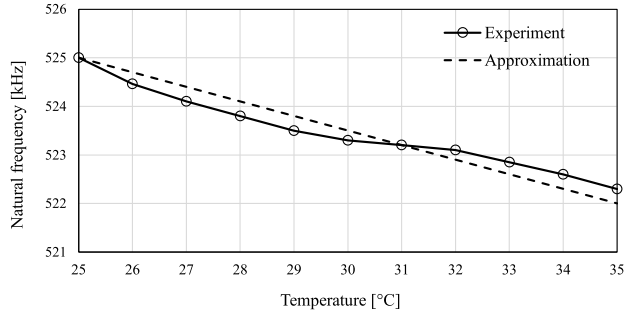

FIGURE 7. Variation in the natural frequency of the stator as the temperature increases.

the micro-ultrasonic motor cannot generate inherent performance at the non-resonant state, a controller that tracks the natural frequency and keep the frequency ratio z in (11) equal to 1 is required.

B. CONTROLLER SELECTION

In the frequency-velocity characteristic (Fig. 5), the angular velocity peaks at the resonant frequency, which is treated as an optimal state. A controller that can converge the output of a system to the optimal state is necessary. The majority of adaptive controllers are model-dependent controllers designed for plants with known setpoints or tracking trajectories to the optimal state. Typically, these setpoints or trajectories are initially determined from the system dynamic model and got updated by real-time system optimization [28]. On contrary, another class of adaptive controllers is model-free like the extremum seeking controller (ESC) which can drive the system to optimal conditions without any prior knowledge about the process model [29], [30], yet provides desirable performance. This controller has a simple structure, a high robustness performance, and a fast convergence rate [31], and can also adapt to the change in plant dynamics.

In the past few years, many researchers have presented several schemes of extremum seeking control for nonlinear systems [30], [32], [33], [34]. The most two known approaches are perturbation-based and model-based ESC. On the one hand, a perturbation-based ESC adapts excitation by an external signal approach to find the unknown optimal operating condition of the plant. This technique optimizes the objective function by online measurement while considering that the input-to-output map is not known at all and that the estimation of derivatives of this map is done directly. It is simple and efficient as long as the transient response of the objective function is guaranteed to be on the right pass of optimization. Its drawbacks are mainly related to that it relies too much on measured parameters and that the perturbation frequency must be slow. Many approaches have been proposed to improve the convergence rate of the perturbation-based ESC. For example, a dual-mode ESC and a phase compensator was introduced in [35] to neutralize the phase shift introduced by the system dynamics to the perturbation signal.

On the other hand, a model-based ESC is more convenient for systems with an accurate dynamical model even though some of its parameters are uncertain. It combines optimum search and adaptive control to guarantee the objective function's convergence to the optimum operating point. It requires explicit knowledge of the mathematical model of the plant, the objective function and its gradient, which may not be available for some systems. The literature is rich with many engineering applications where ESC is dominant, such as automotive applications [36], [37], mobile sensor networks [38], and fuel cell control in power plants [39].

Since real-time accurate speed measurements are used in the computations of our systems, and since the proposed model has some linearity assumptions around the operating range and some uncertainty, we adapt the perturbation-based ESC as the adaptive control scheme for the proposed closed-loop feedback system. The ESC algorithm could handle the non-linear constraints imposed by the temperature fluctuations inherently. With the driving frequency as a manipulated variable, the ESC is implemented to maximize a given objective that is defined as the rotor's maximum angular velocity as follows:

$$J = \Omega_{max} \tag{21}$$

Fig. 8 shows the schematic diagram of the ESC. The ESC aims to calculate the gradient of the objective function, and it continuously updates the control parameters to make the objective function maximum throughout the following three main processes.

1) Modulation process: The parameter being optimized is perturbed with a sinusoidal signal of amplitude A

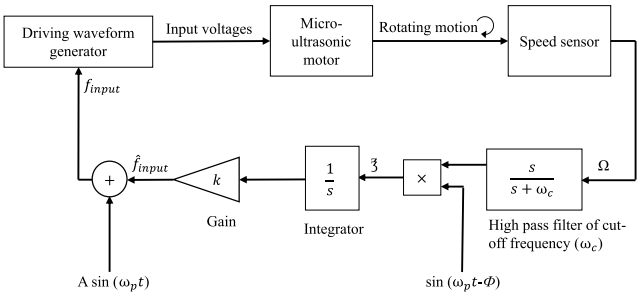

FIGURE 8. Block diagram of the ESC controller for optimum angular velocity tracking.

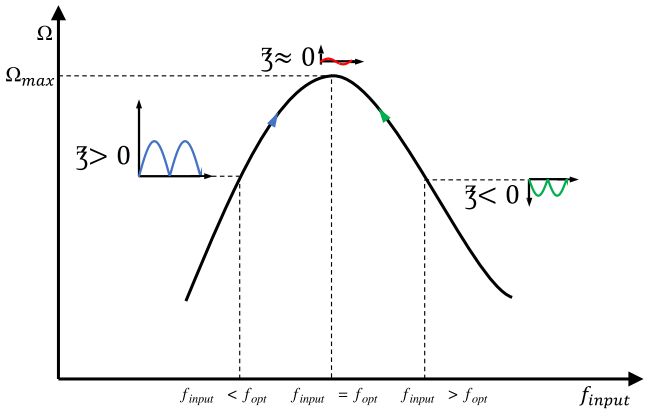

FIGURE 9. ESC localization technique.

and frequency ω_p. In our case, the signal is induced to the input driving frequency $\hat{f}_{input}$ as it is the parameter being optimized as

$$f_{input} = \hat{f}_{input} + A\ \sin(\omega_p\, t) \tag{22}$$

The system's response to the input signal is the objective function Ω that we target for optimization.

2) Demodulation process: The perturbed signal f_{input} is applied to the system and the associated response Ω is measured. The response is filtered by a high pass filter (HPL) with a cutoff frequency ω_c. The cutoff frequency must be lower than the perturbation frequency ω_p to remove signal bias from the objective function without affecting its value. The gradient of the controller ζ is determined by correlating the filtered response with another sinusoidal perturbation having a unit amplitude and the same frequency as ω_p. Thus,

$$\zeta = \text{HPL}(\Omega) \times \sin(\omega_p\, t - \phi) \tag{23}$$

where ϕ is the delayed time imposed by the system dynamics. The sign of the gradient indicates the current controller position compared to the optimum point as indicated in Fig. 9. If ζ is positive, the current driving frequency is lower than the natural frequency of the system. On the contrary, if ζ is negative, the current driving frequency is higher than the natural frequency.

3) Parameter update process: The gradient is integrated over time and multiplied by a gain K to get a faster convergence. Updating the control parameter at time step n can be computed as follows:

$$\hat{f}_{input}(n) = \hat{f}_{input}(n-1) + K \int \zeta\ dt \tag{24}$$

The convergence rate of the driving frequency to the optimum frequency is proportional to the slope of the objective function. In other words, the integral gradient changes at a higher rate when Ω is far from the maximum value, while the steps become finer in the neighborhood of the optimum value Ω_{max}. At this point, the gradient stays almost constant. Reached to the optimum value Ω_{max}, f_{input} oscillates around the current value until the system dynamics change again; the ESC sweeps for the new optimum driving frequency. Table 2 summarizes the parameters of the ESC. The frequencies ω_p and ω_c are set lower than the parameters of the operating system to prevent any interference. The sampling frequency is limited by the response time of the control circuits. The gain K is optimized to get an appropriate response within the working domain of the motor while considering the time-varying nonlinear characteristics of the motor. In other words, a too-fast convergence may lead to unstable condition for the motor and even meets with a sudden stop.

TABLE 2. ESC parameters identification.

Parameter	Symbol	Value
Perturbed frequncy	ω_p	300 Hz
Cutoff frequency	ω_c	240 Hz
Perturbed amplitude	A	200 Hz
Gain	K	350
Sampling frequency		4000 Hz

IV. EXPERIMENT

A. MOTOR-SENSOR SYSTEM

Fig. 10(a) shows a prototype of a micro-ultrasonic motor. The stator is composed of a phosphor bronze cube with a side length of 2 mm, and at the center, there is a hole with a diameter of 1.4 mm. The piezoelectric elements are made of hard material with a high-quality factor (C-213, Fuji ceramics, Japan) and are polarized in the thickness direction. The four piezoelectric plates with a dimension of 2 mm × 1.6 mm and a thickness of 0.6 mm are bonded to the four surfaces of the stator by a conductive adhesive. The length of the rotor passing through the stator hole measures approximately 5 mm (Fig. 10(a)).

To construct a closed-loop system, an internal sensor that can detect the angular velocity is essential. A tiny sensor must have been selected for the closed-loop system to not spoil the advantage of the micro-ultrasonic motors, but there were no commercially available sensors smaller than the size of the micro-ultrasonic motor. Recently, one of the leading sensor companies provided us with the smallest tunneling magneto resistance (TMR) sensor (TAS2240-YIAA, TDK Corp, Ltd, Japan). It is capable of detecting 360° of rotation

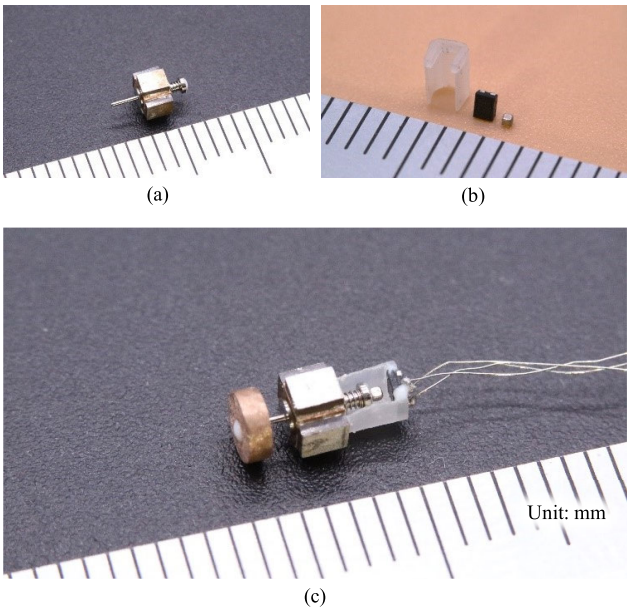

FIGURE 10. (a) The prototype of micro-ultrasonic motor. (b) Components of the sensor system. From the left; the bracket, the TMR sensor, and a neodymium permanent magnet. (c) The motor-sensor system, in which the TMR sensor and the magnet are attached to the bracket and the rotor, respectively.

angle despite its tiny size of 1.4 mm × 1 mm × 0.6 mm, which is very suited for the micro-ultrasonic motor.

Fig. 10(b) shows the components of the sensor system: from the left; a bracket, the TMR sensor, and a tiny magnet. The magnet is a cubic neodymium permanent magnet with a size of 0.5 mm × 0.5 mm × 0.5 mm (Niroku Manufacturing, Tokyo, Japan). Fig. 10(c) shows the motor-sensor system. The magnet is attached to the end of the rotor and spins with the rotor together. The bracket printed by a 3D printer (ProJet 3510HD Plus, 3D Systems Co., USA) holds the TMR sensor near the tiny magnet. When the motor is driven, the tiny magnet spinning with the rotor changes the direction of the magnetic field. The TMR sensor detects the alteration of the magnetic field and outputs a sinusoidal analog voltage corresponding to the change. We can calculate the angular displacement by converting the analog voltage to the angle.

To confirm the accuracy of the TMR sensor, we measure the open-loop angular velocity of the motor with the TMR sensor as an internal sensor, and simultaneously, the high-speed camera records the same motion as an external sensor. Fig. 11 shows the time-history response of the angular velocity for a period of 10 s. The angular velocity recorded by the TMR sensor is well accorded with that recorded by the high-speed camera. Besides, Fig. 11 shows the steady-state error; that is, after reaching the peak at the initial time, the angular velocity gradually decreases. This is because the temperature rise affects the stiffness of the piezoelectric material and the natural frequency of the stator. This steady-state error will be removed in the following sections.

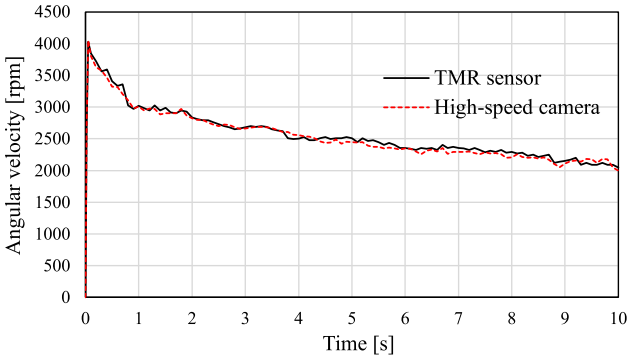

FIGURE 11. The steady-state error of the micro-ultrasonic motor caused by the temperature rise. The output of the TMR sensor (internal sensor) is accorded to that of the high-speed camera (external sensor).

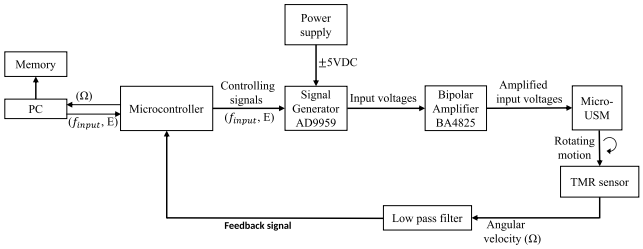

FIGURE 12. The block diagram of the speed control system for the micro-ultrasonic motor.

B. CLOSED-LOOP SYSTEM

Fig. 12 shows the block diagram of the closed-loop control system consisting of the motor, the sensor, the motor driver, and the controller. In general, waveform generators can be controlled by communication with other external devices, but the response time is more than 10 ms. To obtain a quick response, a multichannel direct digital synthesis (DDS) board (AD 9959, Analog Devices Corp., USA) is employed to generate input signals. This board has four channels at up to 500 MSPS, and all of the channels can independently control the amplitude, the frequency, and the phase. The response time to set the output of the board is measured as 0.15 ms, which minimizes the delay time imposed by the system dynamics. The output voltages from the DDS board are amplified by power amplifiers (BA4825, NF Corp.), and the resultant voltages are applied to the motor. The microcontroller (Arduino Uno, Arduino Co., Italy) receives the feedback signal from the sensor, then sends it to MATLAB Simulink program on the PC where all ESC steps are applied. The updated driving frequency f_{input} is then sent back to the microcontroller that, in its turn, forwarded to the DDS board. All of the data are stored in the PC memory for analyses. As the speed sensor operates nearby the high operating frequency of the motor, a low-pass filter is integrated into the system to remove any measuring noises. The cutoff frequency of the filter is higher than the perturbed frequency ω_p to not affect the measured data.

C. EXPERIMENTAL RESULTS

Two experiments are demonstrated to show the effectiveness and robustness of the ESC under continuous operation.

1) CONSTANT SPEED EXPERIMENT

The main objective is to remove the steady-state error and obtain a stable angular velocity. In this experiment, the ESC is applied to the micro-ultrasonic motor under the same operating condition as the experiment for the velocity-frequency characteristic (Fig. 5). We set the initial driving frequency equal to the natural frequency of the stator ($f_n = 525$ kHz). Fig. 13(a) shows the steady-state response when the motor operates continuously for 10 seconds. The dotted line is the reference determined by the steady-state angular velocity measured in Fig. 5, whereas the solid line is the actual speed. The motor accelerates to the peak speed in 50 ms and then stabilizes at around 3800 rpm for a period of 10 s. If we compare the response of the motor in Fig. 13(a) to that of Fig. 11, it is clearly noticeable how the ESC controller minimizes the steady-state error over the operating time. To stabilize the angular velocity, the ESC localizes the natural frequency of the assembled motor ($f_n = 528$ kHz) after a few iterations, and it continuously sweeps to find the optimum frequency as shown in Fig. 13(b). The optimum driving frequency shifts downward with time. Fig. 13(c) shows the temperature variation of the stator during the motion while its initial temperature was recorded at 25°C. Although the increase in the temperature ($\Delta T = 14$°C) is larger than that in the experiment for modeling the temperature-frequency curve (Fig. 6), the model works well to obtain the stable angular velocity in ESC.

In the view of the energy consumption, it is important to know how the input power behaves during the control. The electrical input power is measured as the product of the input voltages, the current, and the power factor. The induced current is measured for one of the four lines driving the motor; we assume that all the lines flow the same current for computation. Under a constant input voltage, the current supplied to the motor and the power factor are measured by a current probe (CT2, Tektronix Corp., Oregon, USA), and a lock-in amplifier (LI5655, NF Corp., Yokohama, Japan), respectively. Fig. 13(d) shows the electric input power to the motor; it peaks at the transient state, stables at the steady-state, and then increases gradually in the response to the thermal power losses. Similarly, the energy efficiency of the motor can be calculated based on the ratio of the mechanical output to the electrical input power. The mechanical output power is computed as the product of torque and angular velocity. The torque can be obtained from the angular acceleration and moment of inertia at the initial time. The efficiency records a maximum value of 6.3% at the steady-state at the first period of the motion and gradually decreases to 5.1% at 10 s.

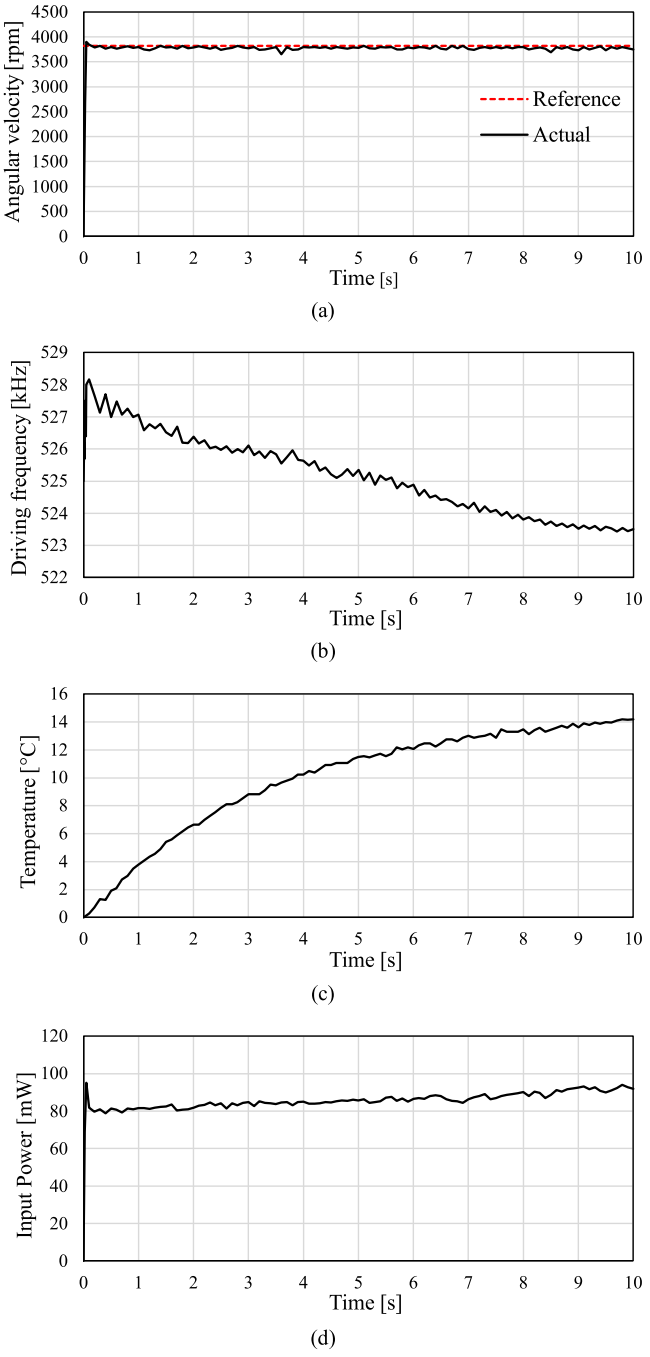

FIGURE 13. Experimental results when ESC is applied to the micro-ultrasonic motor's closed-loop system: (a) The angular velocity, (b) the driving frequency, (c) temperature variation of the stator, and (d) the associated input power.

2) VARIABLE SPEED EXPERIMENT

In case that the manipulated valuable is only the driving frequency, the applicable range of the ESC is limited; therefore, another control parameter is added for further control applications. Using the voltage control is suitable to offer a wide range of speeds. In this subsection, the motor follows variable

input signals of the angular velocity. To follow the variable signals, we add another external voltage control loop (controlled by a PID controller) besides the ESC internal control loop. The PID controller manipulates the input volts which are proportional to the angular velocity in a roughly linear layout as previously shown in [22]. The PID controller was designed and tuned using the online closed-loop auto-tuning toolbox of the MATLAB Simulink program. By executing a trigger test into the controller output, the frequency response of the system can be estimated. The controller's gains are tuned at $K_p = 0.03613$, $K_i = 6.13$, and $K_d = 0.00103$. In such an arrangement, the signal of the TMR sensor is fed back to both controllers simultaneously. Due to deadzone issues [7], the minimum saturation level for PID is set to 60 V_{p-p} while the maximum is set to 120 V_{p-p} to avoid excessive heating.

a: STEPWISE SQUARE WAVE COMMAND

In this experiment, the motor follows a series of stepwise commands of the angular velocity. Fig. 14(a) shows that both controllers drive the motor to match the reference speed without overshoot and steady-state error. The dotted line indicates the input command reference while the solid line refers to the actual motor speed. A slight variation in the steady-state speed is observed due to the perturbed signal of the ESC, although the speed fluctuation is minimized after the transient state. Fig. 14(b) magnifies a step response. It demonstrates a good agreement between the reference and measured trajectories. The steady-state speed overlaps the reference, except for the transient time.

In this experiment, the driving frequency is initially set at $f_n = 525$ kHz and we program the ESC to restore this value as the motor stops during the operation. Fig. 14(c) shows the optimum driving frequency localized by ESC while the motor follows the stepwise input. The frequency downshifts at a proportional rate to the angular velocity. The result means that manipulating the voltage amplitude is independent from the frequency shift.

b: SINUSOIDAL WAVE AND TRIANGULAR WAVE COMMANDS

Other variable input commands are also tested to verify the feasibility of using the dual-mode control structure. A sine wave command of 60 Hz frequency and 500 rpm amplitude is initially evaluated, then a triangular wave command of 100 Hz frequency and 2000 rpm peak-to-peak value is examined. Each commanded input is executed continuously for 5 seconds. Due to the deadzone limitation of ultrasonic motors, we set the midline of the sine wave input to be at 2000 rpm, while the lower margin of the triangular wave is set to 1000 rpm. Fig. 15(a) and (b) show the speed response of the motor to match the two prescribed input commands. In both experiments, the motor could track the commanded given inputs efficiently although some speed fluctuations are recorded. Despite the controller's stability, some overshoot can be observed too at the edges occasionally.

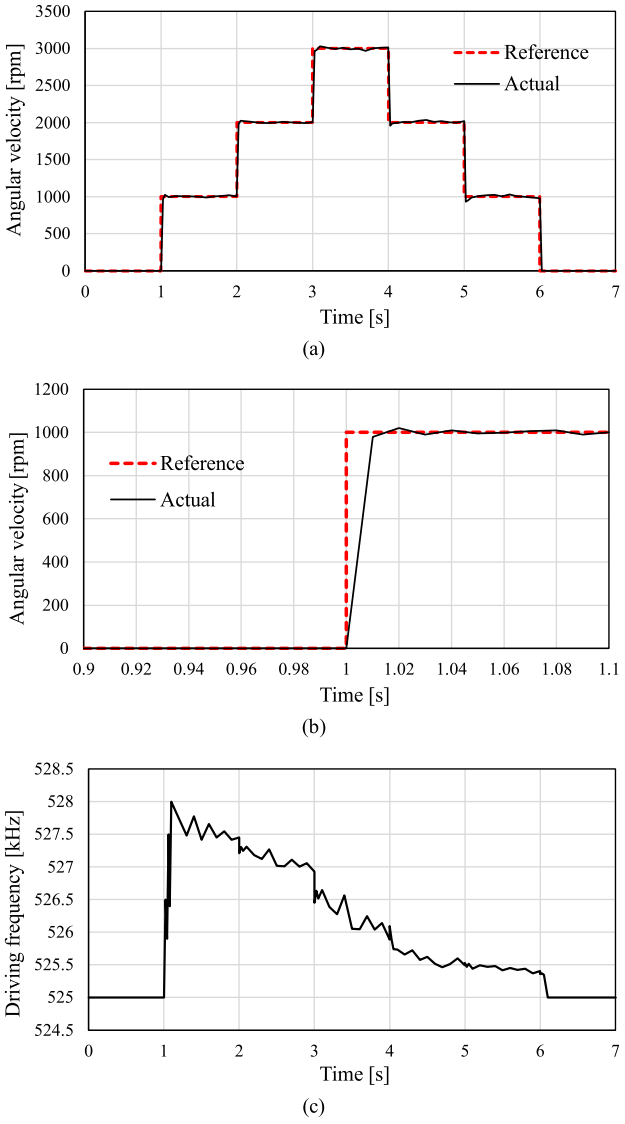

FIGURE 14. Experimental results when two controller loops are applied for tracking stepwise commands. The ECS is controlling the driving frequency while the input voltages are controlled by a PID controller. (a) Comparison between the reference and the actual angular velocity, (b) the transient response, and (c) the driving frequency localized by ESC.

D. PERFORMANCE EVALUATION

Finally, a typical benchmark is to compare the performance of the proposed rotary actuator-sensor system with similar prototypes previously reported by other researchers. Actually, only a few comparable-sized motor-sensor systems have been shown in the past 10 years. For example, a miniature ultrasonic motor that employs a magnetic sensor was reported in [40]. It is as small as our system, but it appears that this study has not been continued afterward. Another prototype that employs the deformation of one piezoelectric plate as the feedback sensing element was reported in [41]. Seeing the motor market, several commercial products (e.g., M3-RS, Newscale Tech. ltd., USA) are released for appli-

TABLE 3. Comparison between the proposed rotary actuator-sensor system with similar prototypes.

Reference	Size [mm^3]	Feedback sensor	Torque [μNm]	Op. frequency [kHz]	Op. volt [V_{p-p}]	Max. angular velocity [rpm]
T. Kanda et al. [42]	2.6× 2.6 × 9.6	Magnetic sensor	2.87	30.6	60	552
S. Toyama et al. [43]	3× 3 × 8.4	Deformation of one PZT plate	52	250.75	180	3300
Squiggle motor (M3-RS) [44]	12 × 22 × 16*	Magnetic sensor	40	N/A	N/A	183
This work	3.2× 3.2 × 5	Magnetic sensor	60 [22]	528	100	3800

*Including a built-in motor driver and a controller

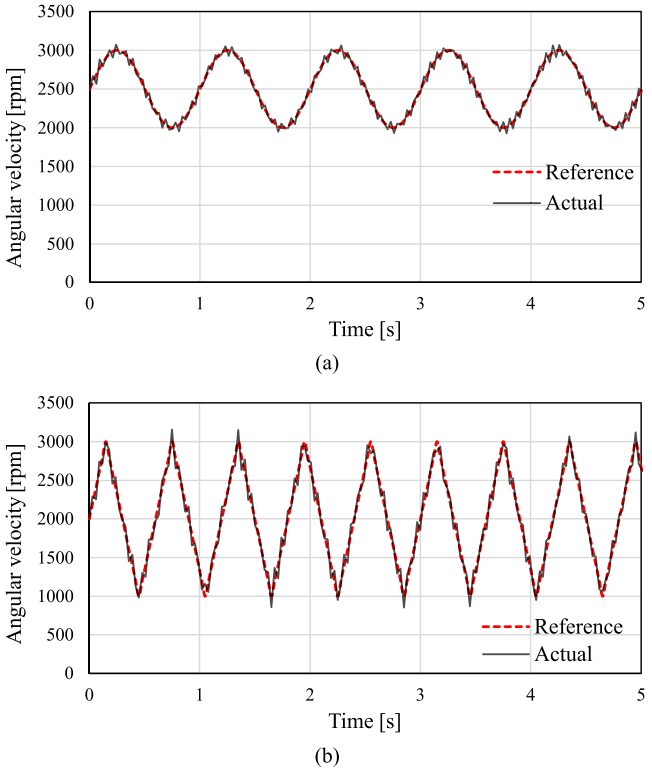

FIGURE 15. Speed response by dual control scheme (ESC and PID) under variable speed commands. (a) Sinusoidal wave command input. (b) Triangular wave command input.

cations. Although this system contains a motor driver in addition to the actuator and sensor, it still results in a compact size [42].

Table 3 summarizes the size, feedback sensing technique, stall torque, operating frequency, operating volts, and the maximum angular velocity of the motors. With a more compact size, Table 3 demonstrates the superiority of the proposed system over all comparable prototypes in terms of overall size, stall torque, and maximum angular velocity.

V. CONCLUSION

In this paper, we designed a suitable controller to cope with the nonlinear and time-varying behavior of the micro-ultrasonic motor. The controller is based on the extremum seeking controller approach that features design simplicity and a high convergence rate. To clarify the nonlinear behavior of the ultrasonic motors, their theory of operation was briefly explained along with the effect of temperature variation on the dynamic characteristic of the motors. To implement the controller, a special hardware setup that consists of various fast response components including a new compact feedback system was built and tested. The size of the new feedback measurement system sensor is very compact compared to other systems in the market, leading to favor for its usage in micro-scale mechatronics and robotics applications.

Finally, by applying the proposed ESC to a micro-ultrasonic motor, the motor operates at its maximum velocity for 10 seconds as the controller continuously localizes the optimum driving frequency. When combined with an external voltage control loop, the applicable range of the ESC was extended and the motor could follow prescribed increasing or decreasing variable commanded angular velocities efficiently.

Final results have revealed that despite running at a constant angular velocity, other associated problems in micro ultrasonic motors such as efficiency improvement are still not fully addressed. Still, we have achieved one step ahead in fully controlling the nonlinear characteristics of ultrasonic motors. Future work will address these challenges and will study the effect of combining input voltages and frequency as the control parameters for the ESC, a system well known as the hybrid or dual control approach. Other model-free adaptive control strategies will be also investigated for the proposed system in the next study. Longer operating periods will also be considered, and that will cover other operating factors affected by the temperature such as the coefficient of friction at stator-rotor interference. Other non-linear properties of ultrasonic motors such as hysteresis will be also investigated for more performance improvement. We also plan to consider the effect of torque ripples or torque fluctuations on

the constant speed controller approach. Finally, we will also consider adjusting the aggressiveness of the controller based on auto-tuning algorithms.

ACKNOWLEDGMENT

The authors would like to thank TDK Corporation for their support on the TMR sensor.

REFERENCES

[1] E. P. Furlani, *Permanent Magnet and Electromechanical Devices: Materials, Analysis, and Applications*. New York, NY, USA: Academic, 2001.
[2] K. Dermitzakis, J. P. Carbajal, and J. H. Marden, "Scaling laws in robotics," *Proc. Comput. Sci.*, vol. 7, pp. 250–252, Jan. 2011.
[3] T. Morita, "Miniature piezoelectric motors," *Sens. Actuators A, Phys.*, vol. 103, no. 3, pp. 291–300, Feb. 2003.
[4] T. Mashimo and S. Izuhara, "Review: Recent advances in micromotors," *IEEE Access*, vol. 8, pp. 213489–213501, 2020.
[5] I. A. Renteria Marquez and V. Bolborici, "A dynamic model of the piezoelectric traveling wave rotary ultrasonic motor stator with the finite volume method," *Ultrasonics*, vol. 77, pp. 69–78, May 2017.
[6] T. Sattel, "Dynamics of ultrasonic motors," Ph.D. thesis, Dept. Appl. Mech., Technische Universität Darmstadt, Germany, 2002.
[7] G. Bal and E. Bekiroglu, "A highly effective load adaptive servo drive system for speed control of travelling-wave ultrasonic motor," *IEEE Trans. Power Electron.*, vol. 20, no. 5, pp. 1143–1149, Sep. 2005.
[8] T. Mashimo and K. Terashima, "Dynamic analysis of an ultrasonic motor using point contact model," *Sens. Actuators A, Phys.*, vol. 233, pp. 15–21, Sep. 2015.
[9] J. Maas, T. Schulte, and N. Frohleke, "Model-based control for ultrasonic motors," *IEEE/ASME Trans. Mechatronics*, vol. 5, no. 2, pp. 165–180, Jun. 2000.
[10] S. Li, W. Ou, M. Yang, C. Guo, C. Lu, and J. Hu, "Temperature evaluation of traveling-wave ultrasonic motor considering interaction between temperature rise and motor parameters," *Ultrasonics*, vol. 57, pp. 159–166, Mar. 2015.
[11] Q. Lv, Z. Yao, L. Zhou, and L. Pan, "Effect of temperature rise on characteristics of a standing wave ultrasonic motor," *J. Intell. Mater. Syst. Struct.*, vol. 30, no. 6, pp. 855–868, Apr. 2019.
[12] S. Shi, H. Xiong, Y. Liu, W. Chen, and J. Liu, "A ring-type multi-DOF ultrasonic motor with four feet driving consistently," *Ultrasonics*, vol. 76, pp. 234–244, Apr. 2017.
[13] M. A. Tavallaei, S. F. Atashzar, and M. Drangova, "Robust motion control of ultrasonic motors under temperature disturbance," *IEEE Trans. Ind. Electron.*, vol. 63, no. 4, pp. 2360–2368, Apr. 2016.
[14] Z. Fang, T. Yang, Y. Zhu, S. Li, and M. Yang, "Velocity control of traveling-wave ultrasonic motors based on stator vibration amplitude," *Sensors*, vol. 19, no. 23, p. 5326, Dec. 2019.
[15] S. Makarem, B. Delibas, and B. Koc, "Data-driven tuning of PID controlled piezoelectric ultrasonic motor," *Actuators*, vol. 10, no. 7, p. 148, 2021.
[16] S. Jingzhuo, H. Wenwen, and Z. Ying, "T–S fuzzy control of travelling-wave ultrasonic motor," *J. Control, Autom. Electr. Syst.*, vol. 31, no. 2, pp. 319–328, 2020.
[17] F. Z. Kebbab, D. E. C. Belkhiat, D. Jabri, and S. Belkhiat, "Frequency speed control of rotary travelling wave ultrasonic motor using fuzzy controller," *Eng., Technol. Appl. Sci. Res.*, vol. 8, no. 4, pp. 3276–3281, Aug. 2018.
[18] A. Mustafa, T. Sasamura, and T. Morita, "Robust speed control of ultrasonic motors based on deep reinforcement learning of a Lyapunov function," *IEEE Access*, vol. 10, pp. 46895–46910, 2022.
[19] S. Jingzhuo and W. Huang, "Model reference adaptive iterative learning speed control for ultrasonic motor," *IEEE Access*, vol. 8, pp. 181815–181824, 2020.
[20] G. Yan, "Design of adaptive sliding mode controller applied to ultrasonic motor," *Assem. Autom.*, vol. 42, no. 1, pp. 147–154, Jan. 2022.
[21] R. Y. Hutama, M. M. Khalil, and T. Mashimo, "A millimeter-scale rolling microrobot driven by a micro-geared ultrasonic motor," *IEEE Robot. Autom. Lett.*, vol. 6, no. 4, pp. 8158–8164, Oct. 2021.
[22] M. M. Khalil and T. Mashimo, "Caterpillar-inspired insect-scale climbing robot using dry adhesives," *IEEE Robot. Autom. Lett.*, vol. 7, no. 3, pp. 7628–7635, Jul. 2022.
[23] E. T. K. Chiang, T. Urakubo, and T. Mashimo, "Lift generation by a miniature piezoelectric ultrasonic motor-driven rotary-wing for pico air vehicles," *IEEE Access*, vol. 10, pp. 13210–13218, 2022.
[24] T. Mashimo, "Miniature preload mechanisms for a micro ultrasonic motor," *Sens. Actuators A, Phys.*, vol. 257, pp. 106–112, Apr. 2017.
[25] S. S. Rao and F. F. Yap, *Mechanical Vibrations*, 5th ed. Upper Saddle River, NJ, USA: Pearson Education, 2010.
[26] E. Bekiroglu, "Ultrasonic motors: Their models, drives, controls and applications," *J. Electroceram.*, vol. 20, nos. 3–4, pp. 277–286, Aug. 2008.
[27] Z. Li, H. Zhao, S. Che, X. Chen, and H. Sun, "Analysis of preload of three-stator ultrasonic motor," *Micromachines*, vol. 13, no. 1, p. 5, Dec. 2021.
[28] D. Dehaan and M. Guay, "Extremum-seeking control of state-constrained nonlinear systems," *Automatica*, vol. 41, no. 9, pp. 1567–1574, 2005.
[29] J. I. Poveda and M. Krstic, "Nonsmooth extremum seeking control with user-prescribed fixed-time convergence," *IEEE Trans. Autom. Control*, vol. 66, no. 12, pp. 6156–6163, Dec. 2021.
[30] G. Lara-Cisneros, D. Dochain, and J. Alvarez-Ramírez, "Model based extremum-seeking controller via modelling-error compensation approach," *J. Process Control*, vol. 80, pp. 193–201, Aug. 2019.
[31] M. Guay and D. Dochain, "A proportional-integral extremum-seeking controller design technique," *Automatica*, vol. 77, pp. 61–67, Mar. 2017.
[32] D. Dochain, M. Perrier, and M. Guay, "Extremum seeking control and its application to process and reaction systems: A survey," *Math. Comput. Simul.*, vol. 82, no. 3, pp. 369–380, Nov. 2011.
[33] Y. Tan, W. H. Moase, C. Manzie, D. Nešić, and I. M. Mareels, "Extremum seeking from 1922 to 2010," in *Proc. 29th Chin. control Conf.*, Jul. 2010, pp. 14–26.
[34] D. Nesic, A. Mohammadi, and C. Manzie, "A framework for extremum seeking control of systems with parameter uncertainties," *IEEE Trans. Autom. Control*, vol. 58, no. 2, pp. 435–448, Feb. 2013.
[35] M. Krstić, "Performance improvement and limitations in extremum seeking control," *Syst. Control Lett.*, vol. 39, no. 5, pp. 313–326, Apr. 2000.
[36] E. Dinçmen, B. A. Güvenç, and T. Acarman, "Extremum-seeking control of ABS braking in road vehicles with lateral force improvement," *IEEE Trans. Control Syst. Technol.*, vol. 22, no. 1, pp. 230–237, Jan. 2012.
[37] D. Popovic, M. Jankovic, S. Magner, and A. R. Teel, "Extremum seeking methods for optimization of variable cam timing engine operation," *IEEE Trans. Control Syst. Technol.*, vol. 14, no. 3, pp. 398–407, May 2006.
[38] M. S. Stankovic and D. M. Stipanovic, "Stochastic extremum seeking with applications to mobile sensor networks," in *Proc. Amer. Control Conf.*, 2009, pp. 5622–5627.
[39] N. Bizon, "On tracking robustness in adaptive extremum seeking control of the fuel cell power plants," *Appl. Energy*, vol. 87, no. 10, pp. 3115–3130, Oct. 2010.
[40] T. Kanda, H. Maeda, and K. Suzumori, "A micro ultrasonic motor controlled by using a built-in micro magnetic encoder," in *Proc. IEEE/ASME Int. Conf. Adv. Intell. Mechatronics*, Jul. 2010, pp. 1029–1034.
[41] S. Toyama and U. Nishizawa, "Mesh robot developed by micro ultrasonic motor," in *Proc. ACTUATOR 16th Int. Conf. New Actuat.*, Jun. 2018, pp. 1–4.
[42] *Website of New Scale Technologies*. Accessed: Jan. 18, 2023. [Online]. Available: https://www.newscaletech.com/micro-motion-modules/m3-rs-rotary-smart-stages/

MOHAMED M. KHALIL (Graduate Student Member, IEEE) received the B.S. and M.S. degrees in mechanical engineering from Arab Academy for Science, Technology and Maritime Transport-Cairo Campus, Egypt, in 2012 and 2018, respectively. He is currently pursuing the Ph.D. degree in mechanical engineering with Toyohashi University of Technology, Japan. He has conducted some research for his master's thesis at Sapienza University, Italy, in 2017. He is with Arab Academy for Science, Technology and Maritime Transport, as a T. A., since his graduation. His research interests include micro piezoelectric actuators, control design, and insect-scale robots.

NAOYA MASUDA was born in 1999. He received the B.E. degree from Toyohashi University of Technology, Japan, in 2022, where he is currently pursuing the master's degree. His research interest includes micro piezoelectric actuators.

KOTARO TAKAYAMA received the Ph.D. degree from the Department of Biological and Environmental Engineering, Graduate School of Agricultural and Life Science, The University of Tokyo, Japan, in 2004. He is currently a Professor with the Mechanical Engineering Department, Toyohashi University of Technology, Toyohashi, Japan. Throughout his academic carrier, he received 18 awards for his publications and scientific works.

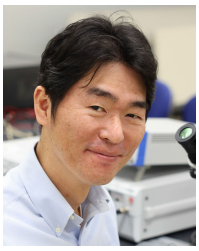

TOMOAKI MASHIMO (Member, IEEE) received the Ph.D. degree in mechanical engineering from Tokyo University of Agriculture and Technology, Fuchu, Japan, in 2008. He was a Robotics Researcher with the Robotics Institute, Carnegie Mellon University, Pittsburgh, PA, USA, from 2008 to 2010. After being an Assistant Professor (tenure-track) with Toyohashi University of Technology, Toyohashi, Japan, in 2011, he became an Associate Professor, in 2016. He is currently a Professor with the Graduate School of Natural Science and Technology, Okayama University, Japan. His research interests include piezoelectric actuators and robotic applications.